

LETTER TO THE EDITOR

SiO outflows in high-mass star forming regions: A potential chemical clock?★,★★

A. López-Sepulcre¹, C. M. Walmsley¹, R. Cesaroni¹, C. Codella¹, F. Schuller², L. Bronfman³, S. J. Carey⁴, K. M. Menten², S. Molinari⁵, and A. Noriega-Crespo⁴

¹ INAF, Osservatorio Astrofisico di Arcetri, Largo E. Fermi 5, 50125 Firenze, Italy
e-mail: sepulcre@arcetri.astro.it

² Max-Planck-Institut für Radioastronomie, Auf dem Hügel 69, 53121 Bonn, Germany

³ Departamento de Astronomía, Universidad de Chile, Casilla 36-D, Santiago, Chile

⁴ Spitzer Science Center, California Institute of Technology, Mail Code 220-6, Pasadena, CA 91125, USA

⁵ INAF – Istituto Fisica Spazio Interplanetario, V. Fosso del Cavaliere 100, 00133 Roma, Italy

Received 27 September 2010 / Accepted 19 November 2010

ABSTRACT

Context. Some theoretical models propose that O-B stars form via accretion, in a similar fashion to low-mass stars. Jet-driven molecular outflows play an important role in this scenario, and their study can help to understand the process of high-mass star formation and the different evolutionary phases involved.

Aims. Observations towards low-mass protostars so far favour an evolutionary picture in which jets are always associated with Class 0 objects while more evolved Class I/II objects show less evidence of powerful jets. The present study aims at checking whether an analogous picture can be found in the high-mass case.

Methods. The IRAM 30-m telescope (Spain) has been used to perform single-pointing SiO(2–1) and (3–2) observations towards a sample of 57 high-mass molecular clumps in different evolutionary stages. Continuum data at different wavelengths, from mid-IR to 1.2 mm, have been gathered to build the spectral energy distributions of all the clumps and estimate their bolometric luminosities.

Results. SiO emission at high velocities, characteristic of molecular jets, is detected in 88% of our sources, a very high detection rate indicating that there is ongoing star formation activity in most of the sources of our sample. The SiO(2–1) luminosity drops with L_{bol}/M , which suggests that jet activity declines as time evolves. This represents the first clear evidence of a decrease of SiO outflow luminosity with time in a homogeneous sample of high-mass molecular clumps in different evolutionary stages. The SiO(3–2) to SiO(2–1) integrated intensity ratio shows only minor changes with evolutionary state.

Key words. stars: formation – ISM: clouds – ISM: jets and outflows – ISM: molecules

1. Introduction

To understand the formation mechanism of O-B stars, several models which assume high accretion rates (e.g. McKee & Tan 2003) and/or accretion through massive discs (e.g. Krumholz et al. 2005) have been proposed. So far, a number of deeply embedded massive disc/outflow systems (see Cesaroni et al. 2007) have been found, lending support to such models. However, a detailed picture of the different evolutionary phases involved in the process is still lacking.

Jet-driven molecular outflows play an important role in the accretion scenario (Arce et al. 2007; Ray et al. 2007). An evolutionary sequence for the outflows driven by massive protostars has been proposed by Beuther & Shepherd (2005), in which an initially well-collimated jet/outflow gradually evolves into a wide-angle wind as the ionising radiation powered by the central massive stellar object becomes more dominant.

* Based on observations conducted with the IRAM 30-m telescope near Pico Veleta (Granada, Spain), and the Atacama Pathfinder Experiment (APEX) ESO project: 181.C-0885. IRAM is supported by INSU/CNRS (France), MPG (Germany), and IGN (Spain). APEX is a collaboration between the Max-Planck-Institut für Radioastronomie, the European Southern Observatory, and the Onsala Space Observatory.

** Appendices are only available in electronic form at <http://www.aanda.org>

López-Sepulcre et al. (2010; LS10 hereafter) studied a sample of high-mass molecular clumps in different evolutionary stages, in the HCO⁺(1–0), HCN(1–0), and C¹⁸O(2–1) transitions with the IRAM 30-m telescope. The detection of outflows was inferred from the presence of extended non-gaussian wings in the HCO⁺(1–0) spectra, together with the spatial distribution of the blue and red lobes. The results show that molecular outflows are present in 75% of the sources.

Although HCO⁺ can trace molecular outflows, contamination from the infalling envelope makes it difficult to separate the outflow component and determine the collimation degree. Further investigation in a reliable jet tracer is needed. SiO emission is ideal for this purpose, because its formation is attributed to sputtering or vaporisation of Si atoms from grains due to fast shocks (Gusdorf et al. 2008; Guillet et al. 2009), and thus suffers minimal contamination from quiescent or infalling envelopes. While in the low-mass case it has been possible to carry out high-spatial resolution observations in SiO, revealing well-collimated molecular jets (e.g. Gueth et al. 1999), only a few SiO surveys have been made towards high-mass SFRs which include IR-dark sources, representative of the earliest evolutionary phases (e.g. Motte et al. 2007; Sakai et al. 2010). However, an interesting recent study by Jiménez-Serra et al. (2010) shows that the SiO emission towards the IR-dark cloud G35.39–0.33 is extended on parsec scale, suggesting widespread low-mass star formation.

Observations towards low-mass protostars so far point to an evolutionary picture in which jets are always associated with Class 0 objects (e.g. Gueth et al. 1999; Codella et al. 2007), while Class I/II objects show less evidence of powerful jets, consistently with the progressive disappearance of the high-density clump around the young stellar object (YSO). The present study represents a first step to check whether an analogous picture can be found in the high-mass case.

With this in mind, we performed SiO(2–1) and (3–2) single-pointing observations towards the central positions of the LS10 sample, to search for evidence of emission caused by jets and check for evolutionary trends in the outflow detection rate and jet activity.

2. The sample

The sample under study is composed of 57 high-mass, parsec-scale molecular clumps. These include the 48 sources studied by LS10, which were selected from the millimetric surveys carried out by Rathborne et al. (2006), Beuther et al. (2002), Faúndez et al. (2004) and Hill et al. (2005); and 9 ultracompact HII (UC HII) regions selected from the maser and/or continuum centimetric surveys performed by Hofner & Churchwell (1996), Walsh et al. (1998) and Wood & Churchwell (1989).

The sample has been sub-classified into two groups which supposedly represent two different evolutionary stages of the star formation process. These are, from less to more evolved phases: (i) 20 infrared dark (IR-dark) clumps, i.e., not detected at $8\ \mu\text{m}$ with the *Midcourse Space eXperient* (MSX). Many of these are embedded $24\ \mu\text{m}$ sources seen with the Multiband Imaging Photometer of Spitzer (MIPS) on the Spitzer Space Observatory; (ii) 37 infrared loud (IR-loud) clumps, i.e., detected at $8\ \mu\text{m}$ by MSX. Within the IR-loud sub-sample, 24 sources are known to contain at least one UC HII region inside a radius of $\sim 20''$. In addition, UC HII regions have been detected at 3.6 cm with the VLA in 4 IR-dark clumps Battersby et al. (2010).

The following criteria are satisfied by the sources in our sample: (i) $\delta > -15^\circ$; (ii) $M_{\text{clump}} \gtrsim 100 M_\odot$, to prevent contamination by low-mass star forming regions; and (iii) $d < 4.5\ \text{kpc}$, to limit the spread in distances. The last criterion is satisfied by all but 5 IR-dark clumps which were found a posteriori to have distances greater than 4.5 kpc (LS10).

3. SiO observations

The IRAM 30-m telescope near Pico Veleta (Granada, Spain) was used on July 30–31 and August 1–2 2009 to observe our sample in the SiO(2–1) and SiO(3–2) lines, with rest frequencies at 86.85 and 130.3 GHz, respectively.

For each source, single-pointing observations in wobbler mode were made, with a wobbler throw of $120''$ and a total integration time (ON + OFF) varying between 4 and 60 min, depending on the source. All the lines were covered at high spectral resolution using the autocorrelator VESPA.

The data were reduced using the programs CLASS and GREG of the GILDAS software package developed by the IRAM and the Observatoire de Grenoble. The spectra were smoothed to a resolution of $1.5\ \text{km s}^{-1}$ to improve the signal to noise ratio. The typical 1σ rms values of the spectra after smoothing are 0.009 K for the SiO(2–1) line, and 0.011 K for the SiO(3–2) line.

Table 1. Continuum data.

Telescope – Instrument	Wavelength (μm)	Ang. Resol. ($''$)	1σ rms (mJy beam^{-1})
MSX – Spirit III	21.3	20	~ 150
Spitzer – MIPS*	24	6	~ 3
IRAS	60	60	~ 85
Spitzer – MIPS*	70	18	~ 40
IRAS	100	120	~ 300
APEX – LABOCA [†]	850	18	~ 100
IRAM 30-m – MAMBO [‡]	1200	11	$\sim 10\text{--}15$
SEST 15-m – SIMBA [‡]	1200	24	$\sim 40\text{--}150$

Notes. (*) Spitzer Galactic plane MIPS GAL survey (Carey et al. 2005, 2009). (†) APEX Telescope Large Area Survey of the Galaxy (ATLASGAL) survey (Schuller et al. 2009). (‡) Millimetre surveys cited in Sect. 2.

4. Continuum observations

Continuum data at different wavelengths, ranging from mid-IR to 1.2 mm, have been gathered in order to characterise the emission of the clumps from their spectral energy distributions (SEDs). Table 1 summarises the telescopes, instruments, wavelengths, angular resolution, and sensitivity of the data.

5. Results and discussion

5.1. Spectral energy distributions

Single-temperature, modified black body functions have been fitted to the SEDs of our sources to estimate their dust temperatures, masses (derived from the dust temperature and the dust continuum emission at 1.2 mm integrated over the whole clump), and bolometric luminosities (Table A.1). This has been possible for 47 of the observed clumps. For the remaining 10 sources, data from fewer than three of the surveys listed in Table 1 were available and thus the fit was not sufficiently reliable. While the single-temperature modified black body is a simplified model, it is sufficient for our purposes and it characterises the global properties of our dusty clumps.

The luminosities ($\sim 10^3\text{--}10^6 L_\odot$) and masses (~ 50 to $\sim 1000 M_\odot$) derived are typical of high-mass SFRs. The IR-dark clumps are on average colder and less luminous (by about an order of magnitude), although their masses are comparable to those of the IR-loud clumps. We note that the bolometric luminosities obtained for the sources using IRAS data represent upper limits to the actual luminosities in that there are often several sources within one IRAS beam. Similarly, upper limit luminosities were derived for 5 IR-dark sources for which only upper limits were available at 24 and/or $70\ \mu\text{m}$ emission.

5.2. SiO outflow detection rate

SiO emission has been clearly detected above 3σ in 88% of the sources. We note that, even if the sources with no SiO detection correspond to spectra with σ above the average value, the weakest detection in our sample is well above the 3σ level of the noisiest non-detection, and therefore we do not consider our SiO detection rate to be biased by the sensitivity of the different observed spectra. Out of the 7 non-detections, 6 belong to the IR-loud group, which implies a detection rate of 84% for the IR-loud sub-sample and 95% for the IR-dark sub-sample. These high detection rates are similar to the one reported by Motte et al. (2007) for a population of massive cores inside Cygnus X.

The lines display a wide variety of intensities, widths and shapes. Figure B.2 presents the SiO(2–1) and (3–2) spectra of all

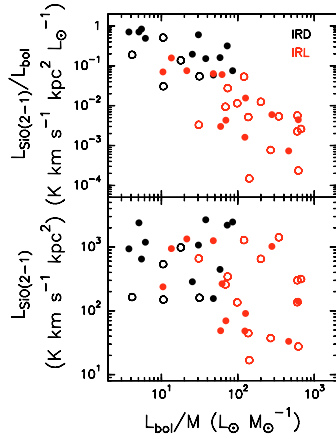


Fig. 1. *Top:* SiO(2–1) to bolometric luminosity ratio, $L_{\text{SiO}(2-1)}/L_{\text{bol}}$, against L_{bol}/M . *Bottom:* SiO(2–1) luminosity, $L_{\text{SiO}(2-1)}$, against L_{bol}/M . IR-dark and IR-loud clumps are marked as black and red circles, respectively. Open circles depict sources for which the derived luminosity represents an upper limit (see Sect. 5.1).

our detected sources. In all the cases the lines have Full Widths at Zero Power (FWZP) of $\sim 10 \text{ km s}^{-1}$ or more. The median FWZP of our sample is 38 km s^{-1} for the SiO(2–1) line, and 45 km s^{-1} for the SiO(3–2) line. On average, IR-dark clumps present broader SiO(2–1) wings than IR-loud clumps, with median values of 49 km s^{-1} for the former and 24 km s^{-1} for the latter. In some cases the SiO line wings extend up to velocities of about $40\text{--}50 \text{ km s}^{-1}$ from the systemic velocity of the clump. Such high velocities point to the presence of molecular outflows, likely caused by jets, and therefore active star formation, in most of our sources. Table A.2 lists the measured SiO(2–1) and (3–2) FWZPs and velocity-integrated intensities for all the observed sources.

There is good agreement between the detection of SiO and the presence of $\text{HCO}^+(1-0)$ outflows as reported by LS10 (Table A.2): 95% of the sources with an HCO^+ outflow present also SiO emission. There are 6 sources with clear SiO emission which have no reported HCO^+ outflow, but they all have SiO spectra with FWZP lower than about 15 km s^{-1} , and $\text{HCO}^+(1-0)$ spectra with similar widths. This is compatible with molecular outflows oriented close to the plane of the sky: the narrowest SiO spectra likely have counterpart $\text{HCO}^+(1-0)$ spectra where the blue and red outflow wings are mixed with the low ambient velocities of the line. Our results therefore confirm that SiO is closely associated with molecular outflows. As an example, Fig. B.1 presents the SiO(2–1) and (3–2) spectra of two of our targets (one IR-loud and one IR-dark), with an overlay of their corresponding $\text{HCO}^+(1-0)$ spectra (LS10).

5.3. Decrease of SiO outflow activity with time

It is reasonable to expect that the bolometric luminosity, L_{bol} , of a molecular clump will increase as time evolves and the high-mass star gradually switches on, while its mass will decrease due to the effect of molecular outflows, winds, and HII regions (e.g. McKee & Tan 2002). Therefore, the luminosity to mass ratio, L_{bol}/M , can be considered to be a time estimator which, in addition, gets rid of distance effects. We will then consider L_{bol}/M to be a measure of time or evolutionary phase, with lower values corresponding to less evolved stages of cluster formation.

From the integrated intensity of the SiO(2–1) line, the SiO(2–1) luminosity, $L_{\text{SiO}(2-1)}$, has been calculated. Figure 1 (top) displays a plot of $L_{\text{SiO}(2-1)}/L_{\text{bol}}$ against L_{bol}/M for the

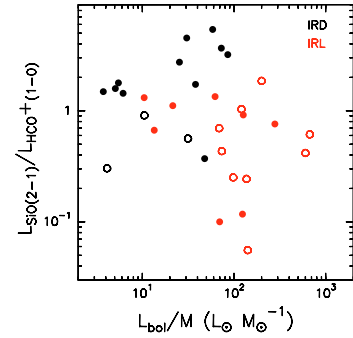


Fig. 2. Ratio of SiO(2–1) luminosity to $\text{HCO}^+(1-0)$ line wing luminosity, $L_{\text{SiO}(2-1)}/L_{\text{HCO}^+(1-0)}$, against L_{bol}/M . The same symbols as in Fig. 1 apply here.

47 sources where the SED could be fitted by a modified black body function (see Sect. 4.1). IR-dark and IR-loud clumps are depicted in black and red, respectively. One notes that the two types of object occupy two distinct areas of the plot. This plot shows that the most luminous SiO outflows are associated with the youngest stages of high-mass star and cluster formation. In the lower panel of Fig. 1, $L_{\text{SiO}(2-1)}$ is plotted instead of $L_{\text{SiO}(2-1)}/L_{\text{bol}}$. We note that the results in the upper panel of Fig. 1 have an inherent bias in that the bolometric luminosity appears both in the denominator of the ordinate and in the numerator of the abscissa. This however is not the case in the lower panel, where nonetheless one observes a dearth of points in the lower left hand corner. Although we do not show it here, a similar trend is found when the outflow terminal velocity is plotted against L_{bol}/M .

The trend seen in Fig. 1 may be interpreted as a decrease in the SiO abundance with time (as suggested by Sakai et al. 2010), a decrease in the jet/outflow mass with time, or a combination of both. In an attempt to discriminate between these possibilities, we present in Fig. 2 a plot of SiO(2–1) to $\text{HCO}^+(1-0)$ luminosity ratio, $L_{\text{SiO}(2-1)}/L_{\text{HCO}^+(1-0)}$, against L_{bol}/M . $L_{\text{HCO}^+(1-0)}$ corresponds to the emission under the line wings defined by LS10. It can be seen that IR-dark sources lie higher in the plot, while high L_{bol}/M sources are on average lower and have greater dispersion in $L_{\text{SiO}(2-1)}/L_{\text{HCO}^+(1-0)}$. This difference between less evolved and more evolved objects favours the interpretation in which SiO abundance decreases with time, since otherwise one would expect all the points in Fig. 2 to cluster around a constant value of $L_{\text{SiO}(2-1)}/L_{\text{HCO}^+(1-0)}$. Moreover, LS10 reported similar outflow masses among the IR-dark and the IR-loud sub-samples, and therefore there is no significant difference in the outflow mass between more evolved and less evolved clumps. Given that SiO is thought to be produced in fast shocks which can be effectively generated by fast collimated jets, this result suggests that the earliest phases of star formation are dominated by well-collimated jets, which gradually de-collimate and lose power. Such a decrease in the SiO outflow luminosity with time seems analogous to what is found for low-mass SFRs (e.g. Gibb et al. 2004), where the most intense SiO emission is detected towards the less evolved Class 0 objects. This similarity between the low-mass and the high-mass regime lends support to the disc accretion models as the mechanism to form high-mass stars.

It could be argued that the SiO emission arising from the high L_{bol}/M sources comes from low-mass YSOs within the region and not from their high-mass neighbours. However, LS10 reported outflow masses and momentum rates consistent with high-mass stars, independently of the evolutionary phase. Therefore, the correlation seen in Fig. 1 most likely

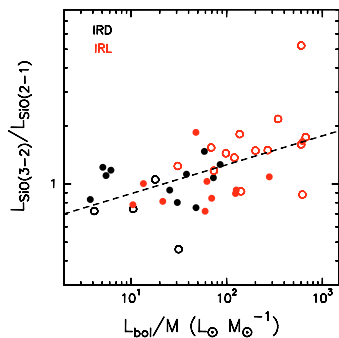


Fig. 3. SiO(3–2) to SiO(2–1) luminosity ratio, $L_{\text{SiO}(3-2)}/L_{\text{SiO}(2-1)}$, against L_{bol}/M . The dashed line represents the best fit to the points (see text). The same symbols as in Fig. 1 apply here.

represents an evolutionary line for molecular outflows driven by massive YSOs, compatible with the scenario proposed by Beuther & Shepherd (2005) in which initially well collimated outflows gradually disappear to make way for a wide-angle wind-dominated outflow. Our result is consistent with the findings of Miettinen et al. (2006), who measured a decrease of the SiO abundance with core temperature in a sample of 15 UC HII regions and concluded that SiO outflows are less frequent in more evolved, warmer cores. Given that our sample, which includes IR-dark sources, presumably covers a wider range of evolutionary phases, this represents the first time that clear evidence of a decrease in jet/outflow activity with time is found in a sample of high-mass SFRs.

A final remark concerns the excitation conditions of the jet environment. We checked for a possible dependence of the SiO(3–2) to SiO(2–1) intensity ratio on velocity, but a well defined trend has not been discerned. Further, we present in Fig. 3 a plot of SiO(3–2) to SiO(2–1) luminosity ratio, $L_{\text{SiO}(3-2)}/L_{\text{SiO}(2-1)}$, as a function of L_{bol}/M . Such a ratio changes by at most a factor 4 over the sampled range of L_{bol}/M . The points follow a weak trend which can be described by the function $L_{\text{SiO}(3-2)}/L_{\text{SiO}(2-1)} = 0.63(L_{\text{bol}}/M)^{0.15}$, with a correlation coefficient of 0.38, obtained from a least squares fit to all the points. Notice, however, that the best fit results depend on whether the open circles (representing upper limits to the bolometric luminosity) are included or not, and therefore the correlation found should be confirmed using a more statistically reliable sample. The trend, if real, suggests that the excitation temperature of the post-shock environment increases only marginally with time, which may be explained by a small increase in density with time. To this end, we used the non-LTE excitation code RADEX with an escape probability formalism for the radiative transfer (Van der Tak et al. 2007) coupled with the LAMDA database (Schöier et al. 2005). Assuming that (i) both SiO lines trace the same region; and (ii) the beam filling factor equals unity, then, for a kinetic temperature between 50 and 150 K, we infer densities between 5×10^4 and 10^6 cm^{-3} . The total SiO column densities lie in the range 10^{12} – 10^{13} cm^{-2} . A more exhaustive study of the level of excitation of SiO would require high angular resolution mapping of higher J transitions.

6. Conclusions

We have observed SiO(2–1) and SiO(3–2) with the IRAM 30-m telescope towards a sample of 57 high-mass molecular clumps

in different evolutionary stages, and characterised their IR and (sub)mm emission using continuum data from the archive and a modified grey body function model to fit their SEDs. High-velocity SiO emission has been detected in 88% of our sample at high velocities, implying star formation is actively taking place in most of our targets. A tight inverse correlation is found between $L_{\text{SiO}(2-1)}/L_{\text{bol}}$ and L_{bol}/M , which is interpreted as the presence of an evolutionary line in which jet activity fades as time evolves. This picture is analogous to what is found in the low-mass regime, which suggests that high-mass stars may form generally via disc accretion as low-mass stars. Our result is consistent with the evolutionary picture suggested by Beuther & Shepherd (2005) for massive molecular outflows. For the first time, evidence of a clear decrease of SiO outflow luminosity with time has been measured in a sample of high-mass star forming clumps in different evolutionary stages, covering both IR-dark and IR-loud clumps. A relatively constant luminosity ratio of SiO(3–2) to (2–1) integrated intensity is found in our sample, suggesting that the post-shock density does not vary greatly. We note, however, that high-angular resolution imaging is necessary to confirm our conclusions.

Acknowledgements. A.L.S. acknowledges support from the FP6 Marie-Curie Research Training Network “Constellation: the origin of stellar masses” (MRTN-CT-2006-035890). L.B. acknowledges support from FONDAP Center for Astrophysics 15010003. We are grateful to the staff of IRAM-Granada for the help provided during the observations at the 30-m telescope. We also thank our referee for his valuable comments and suggestions.

References

- Arce, H. G., Shepherd, D., Gueth, F., et al. 2007, PPV, 245
 Battersby, C., Bally, J., Jackson, J. M., et al. 2010, ApJ, 721, 222
 Beuther, H., & Shepherd, D. 2005, CCSF, 105
 Beuther, H., & Sridharan, T. K. 2007, ApJ, 668, 348
 Beuther, H., Schilke, P., Menten, K. M., et al. 2002, ApJ, 566, 945
 Carey, S. J., Noriega-Crespo, A., Price, S., et al. 2005, BAAS, 37, 1252
 Carey, S. J., Noriega-Crespo, A., Mizuno, D. R., et al. 2009, PASP, 121, 76
 Cesaroni, R., Galli, D., Lodato, G., Walmsley, C. M., & Zhang, Q. 2007, in Protostars and Planets V, 197 (Tucson: Univ. Arizona Press)
 Codella, C., Cabrit, S., Gueth, F., et al. 2007, A&A, 462, L53
 Faúndez, S., Bronfman, L., Garay, G., et al. 2004, A&A, 426, 97
 Gibb, A. G., Richer, J. S., Chandler, C. J., & Davis, C. J. 2004, ApJ, 603, 198
 Gibb, A. G., Davis, C. J., & Moore, T. J. T. 2007, MNRAS, 382, 1213
 Giveon, U., Becker, R. H., Helfand, D. J., & White, R. L. 2005, ApJ, 129, 348
 Gueth, F., & Guilloteau, S. 1999, A&A, 343, 571
 Guillet, V., Jones, A. P., Pineau Des Forêts, G. 2009, A&A, 497, 145
 Gusdorf, A., Cabrit, S., Flower, D. R., et al. 2008, A&A, 482, 809
 Hill, T., Burton, M. G., Minier, V., et al. 2005, MNRAS, 363, 405
 Hofner, P., & Churchwell, E. 1996, A&AS, 120, 283
 Jiménez-Serra, I., Caselli, P., Tan, J. C., et al. 2010, MNRAS, 406, 187
 Krumholz, M. R., McKee, C. F., & Klein, R. I. 2005, ApJ, 618, L33
 López-Sepulcre, C. R., & Walmsley, M. 2010, A&A, 517, A66 (LS10)
 McKee, C. F., & Tan, J. C. 2002, Nature, 416, 59
 McKee, C. F., & Tan, J. C. 2003, ApJ, 585, 850
 Miettinen, O., Harju, J., Haikala, L. K., & Pomré, C. 2006, A&A, 460, 721
 Motte, F., Bontemps, S., Schilke, P., et al. 2007, A&A, 476, 1243
 Rathborne, J. M., Jackson, J. M., & Simon, R. 2006, ApJ, 641, 389
 Rathborne, J. M., Jackson, J. M., Chambers, E. T. et al. 2010, ApJ, 715, 310
 Ray, T., Dougados, C., Bacciotti, F., et al. 2007, PPV, 231
 Sakai, T., Sakai, N., Hirota, T., & Yamamoto, S. 2010, ApJ, 714, 1658
 Schöier, F. L., van der Tak FFS., van Dishoeck, E. F., & Black, J. H. 2005, A&A, 432, 369
 Schuller, F., Menten, K. M., Contreras, Y., et al. 2009, A&A, 504, 415
 Van der Tak, F. F. S., Black, J. H., Schöier, F. L., Jansen, D. J., et al. 2007, A&A, 468, 627
 Walsh, A. J., Burton, M. G., Hyland, A. R., et al. 1998, MNRAS, 301, 640
 Wood, D. O. S., & Churchwell, E. 1989, ApJ, 69, 831

Appendix A: Tables**Table A.1.** Properties of the clumps derived from modified black body fits to their SEDs.

Source	T_{dust} (K)	M (M_{\odot})	L_{bol} (L_{\odot})
05358+3543	76	70	4370
G213.61-12.6*	39	800	113 000
G189.78+0.34*	42	63	8630
G192.60-0.05*	72	100	60 200
18151-1208_1*	75	120	11 800
G18.15-0.28	105	43	33 400
G18.18-0.30	32	55	2640
18223-1243	73	230	16 100
18228-1312	95	240	29 800
G19.27+0.1M2	29	57	1450
G19.27+0.1M1	33	47	2760
18232-1154	53	61	19 800
18236-1205	60	320	3370
G19.61-0.24A*	59	765	264 000
G20.08-0.1	66	410	19 700
18264-1152	59	440	5970
G23.60+0.0M1	21.5	660	3370
18316-0602	48	610	171 000
G23.60+0.0M2	26	58	1780
18317-0513	79	270	16 200
G24.08+0.0M2*	31	93	2930
G24.33+0.1M1	56	460	17 600
G24.33+0.1M4*	41	460	4890
G24.33+0.1M2*	28	400	7190
G24.60+0.1M2	21	390	2420
G24.60+0.1M1	22	140	772
G25.04-0.2M1	20	350	1320
G25.04-0.2M4*	33	210	869
G25.04-0.2M2*	25	100	1060
G28.28-0.35	109	97	45 100
G34.43+0.2M1	42	380	32 700
18507+0121	61	820	17 700
G34.43+0.2M3	35	95	6940
G34.24+0.13	48	51	31 700
18517+0437*	43	400	27 600
19035+0641*	74	46	5830
19095+0930	61	260	52 100
G43.89-0.38*	57	88	53 100
G61.48+0.09A*	66	189	117 000
20216+4107*	72	17	3180
20332+4124	79	180	23 900
22134+5834*	82	55	12 600
22570+5912_1*	82	180	48 400
23033+5951	71*	170	12 500
NGC7538B*	37	6480	200 000
23139+5939*	71	200	24 100
23151+5912*	98	180	121 000

Notes. (*) Sources whose derived luminosities are upper limits (see Sect. 5.1).

Table A.2. Parameters of the SiO(2–1) and (3–2) lines, and HCO⁺ outflow detection.

Sub-class	Source	RA (J2000.0)	Dec (J2000.0)	V_{LSR}^* (km s ⁻¹)	SiO(2–1)		SiO(3–2)		HCO ⁺ outflow? [‡] (Y/N)
					$FWZP^\dagger$ (km s ⁻¹)	$\int F_\nu dv^\ddagger$ (K km s ⁻¹)	$FWZP^\dagger$ (km s ⁻¹)	$\int F_\nu dv^\ddagger$ (K km s ⁻¹)	
IRL	05358+3543	05:39:12.20	+35:45:52.0	-15.8	38.3	6.5	50.2	6.8	Y
IRL	G213.61-12.6	06:07:49.23	-06:22:40.6	10.6	9.2	0.3	5.8	0.3	Y
IRL	G189.78+0.34	06:08:35.35	+20:39:04.3	9.2	15.2	1.1	21.0	2.0	Y
IRL	G192.58-0.04	06:12:52.90	+18:00:35.0	9.1	35.9	1.7	17.0	1.4	Y
IRL	G192.60-0.05	06:12:54.00	+17:59:23.0	7.4	29.2	1.6	23.1	2.6	Y
IRD	18151-1208_2	18:17:50.50	-12:07:55.0	29.8	84.3	5.7	103.1	11.6	Y
IRL	18151-1208_3	18:17:52.30	-12:06:56.0	30.7	–	–	–	–	N
IRL	18151-1208_1	18:17:58.00	-12:07:27.0	33.3	36.3	1.2	31.1	1.7	Y
IRL	G18.15-0.28	18:25:02.41	-13:15:25.7	55.8	–	–	–	–	N
IRD	G18.18-0.30	18:25:07.30	-13:14:23.0	50.0	35.9	1.8	29.8	1.4	Y
IRL	18223-1243	18:25:10.87	-12:42:26.8	45.2	21.2	0.4	13.0	0.3	Y
IRL	18228-1312	18:25:42.35	-13:10:18.1	33.1	15.2	0.4	27.9	0.4	Y
IRD	G19.27+0.1M2	18:25:52.60	-12:04:48.0	26.9	66.3	4.0	51.0	3.7	Y
IRD	G19.27+0.1M1	18:25:58.50	-12:03:59.0	26.5	75.9	6.2	69.9	9.1	Y
IRL	18232-1154	18:26:04.37	-11:52:33.4	24.4	–	–	–	–	–
IRL	18236-1205	18:26:25.41	-12:03:51.4	26.5	51.1	3.0	34.8	2.4	Y
IRL	G19.61-0.24A	18:27:38.16	-11:56:40.2	42.4	51.1	7.8	59.0	17.0	–
IRL	G20.08-0.14	18:28:10.28	-11:28:48.7	42.5	41.9	8.7	50.0	16.2	–
IRL	18264-1152	18:29:14.40	-11:50:21.3	43.9	71.1	6.2	40.1	6.2	Y
IRD	G23.60+0.0M1	18:34:11.60	-08:19:06.0	106.5	73.1	5.0	82.9	6.1	Y
IRL	18316-0602	18:34:20.46	-05:59:30.4	42.5	75.1	8.5	60.3	9.3	Y
IRD	G23.60+0.0M2	18:34:21.10	-08:18:07.0	53.6	85.1	5.6	57.9	4.5	Y
IRL	18317-0513	18:34:25.94	-05:10:48.6	42.0	16.4	0.4	9.8	0.3	N
IRD	G24.08+0.0M2	18:34:51.10	-07:45:32.0	52.0	21.2	0.9	17.0	0.4	Y
IRD	G24.33+0.1M1	18:35:07.90	-07:35:04.0	113.6	49.1	4.8	55.0	5.4	Y
IRD	G24.33+0.1M4	18:35:18.56	-07:37:26.2	114.3	8.4	0.3	–	–	N
IRD	G24.33+0.1M2	18:35:34.50	-07:37:28.0	118.6	33.1	1.6	44.6	1.7	N
IRD	G24.60+0.1M2	18:35:35.70	-07:18:09.0	115.3	53.1	2.1	43.0	2.4	Y
IRD	G24.60+0.1M1	18:35:40.20	-07:18:37.0	53.2	49.9	3.8	67.0	4.2	Y
IRD	G25.04-0.2M1	18:38:10.20	-07:02:34.0	63.8	66.3	4.0	52.1	3.4	Y
IRD	G25.04-0.2M4	18:38:13.70	-07:03:12.0	63.8	18.4	0.7	13.0	0.5	Y
IRD	G25.04-0.2M2	18:38:17.70	-07:02:51.0	63.9	30.0	2.3	24.2	1.7	Y
IRL	G28.28-0.35	18:44:14.20	-04:17:59.0	48.7	8.4	0.3	–	–	N
IRD	G34.43+0.2M1	18:53:18.00	+01:25:23.0	58.1	75.1	14.4	63.0	18.2	Y
IRL	G34.26+0.15	18:53:18.44	+01:14:57.8	58.4	25.2	6.6	24.2	13.4	–
IRL	18507+0121	18:53:19.58	+01:24:37.1	58.2	57.1	7.8	52.1	6.4	Y
IRD	G34.43+0.2M3	18:53:20.40	+01:28:23.0	59.4	85.9	12.9	72.0	13.9	Y
IRL	G34.24+0.13	18:53:21.70	+01:13:37.0	57.2	18.0	0.9	34.0	1.5	N
IRL	18517+0437	18:54:14.30	+04:41:40.0	44.1	13.2	2.4	26.0	3.8	Y
IRD	G34.77-0.6M2	18:56:49.41	+01:23:16.0	42.2	–	–	–	–	N
IRD	G35.39-0.3M4	18:57:07.90	+02:08:23.0	44.6	15.2	0.5	9.0	0.5	N
IRL	G35.20-1.74	19:01:46.40	+01:13:24.5	45.0	33.1	0.7	32.2	1.2	–
IRD	G38.95-0.5M1	19:04:07.40	+05:08:48.0	42.3	32.4	1.8	14.9	1.1	Y
IRL	19035+0641	19:06:01.60	+06:46:43.0	32.8	24.4	1.5	30.0	1.4	Y
IRL	19095+0930	19:11:54.02	+09:35:52.0	43.9	42.3	4.8	55.8	7.1	Y
IRL	G43.89-0.38	19:14:26.07	+09:22:33.9	53.7	41.9	1.4	47.8	7.1	–
IRL	G61.48+0.09A	19:46:49.11	+25:12:48.0	21.5	11.2	0.5	12.0	0.5	–
IRL	G75.78-0.34	20:21:44.01	+37:26:39.4	0.3	36.3	4.4	40.9	6.9	–
IRL	20216+4107	20:23:23.60	+41:17:38.0	-1.6	–	–	–	–	Y
IRL	20332+4124	20:34:59.90	+41:34:49.0	-2.7	–	–	–	–	N
IRL	22134+5834	22:15:09.30	+58:49:06.0	-18.3	–	–	–	–	Y
IRL	22570+5912_2	22:58:58.75	+59:27:29.2	-47.8	12.0	0.5	22.1	0.7	N
IRL	22570+5912_1	22:59:05.90	+59:28:19.0	-45.6	–	–	5.0	0.2	N
IRL	23033+5951	23:05:25.50	+60:08:06.0	-53.1	33.9	2.2	52.9	2.6	Y
IRL	NGC7538B	23:13:45.25	+61:28:10.2	-57.0	38.3	4.3	57.1	5.3	–
IRL	23139+5939	23:16:11.12	+59:55:30.8	-44.1	61.1	4.4	59.0	6.1	Y
IRL	23151+5912	23:17:21.00	+59:28:49.0	-54.5	25.2	0.8	27.1	1.3	Y

Notes. ^(*) Systemic velocity of the clump as measured from the peak velocity of the optically thin H¹³CO⁺(1–0) line, observed simultaneously to SiO(2–1) and SiO(3–2). ^(†) Not detected. ^(‡) No observation made towards this source (see Sect. 2).

Appendix B: Figures

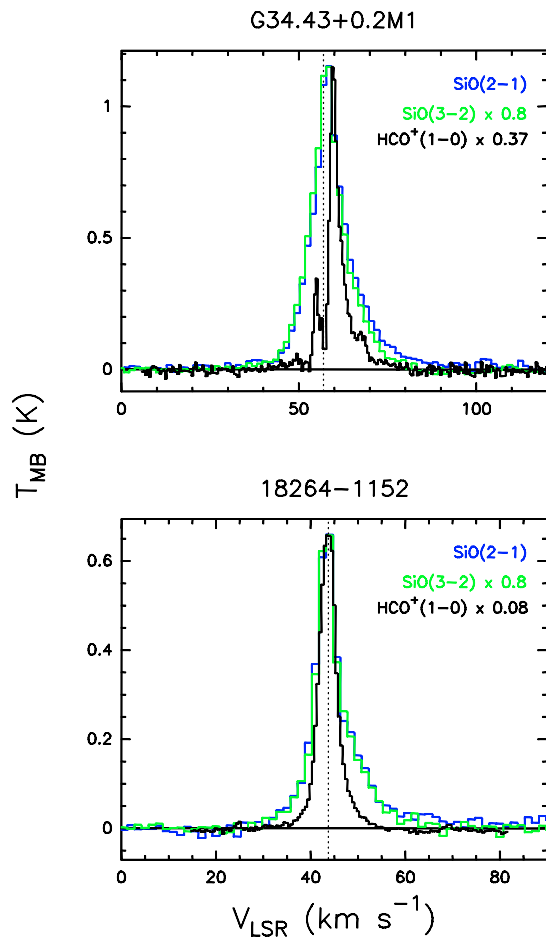


Fig. B.1. SiO(2-1) (*blue*), SiO(3-2) (*green*), and HCO⁺(1-0) (*black*) spectra observed towards the IR-dark source G34.43+0.2M1 and the IR-loud source 18264-1152. The vertical dotted lines mark the systemic velocity of the clump, listed in Col. 5 of Table A.2.

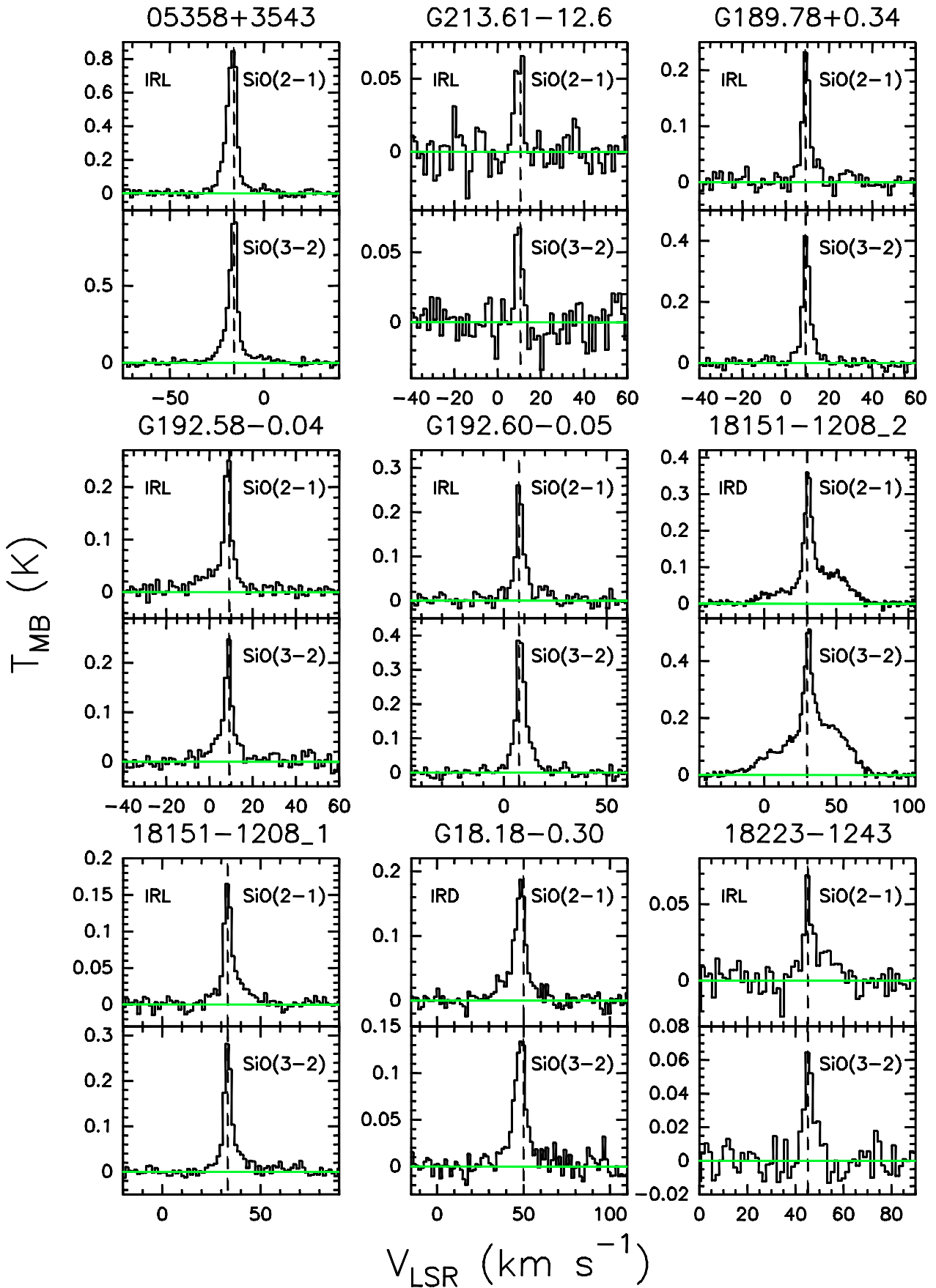


Fig. B.2. SiO(2-1) and (3-2) spectra. The dashed vertical line marks the systemic velocity of the clump, listed in Col. 5 of Table A.2.

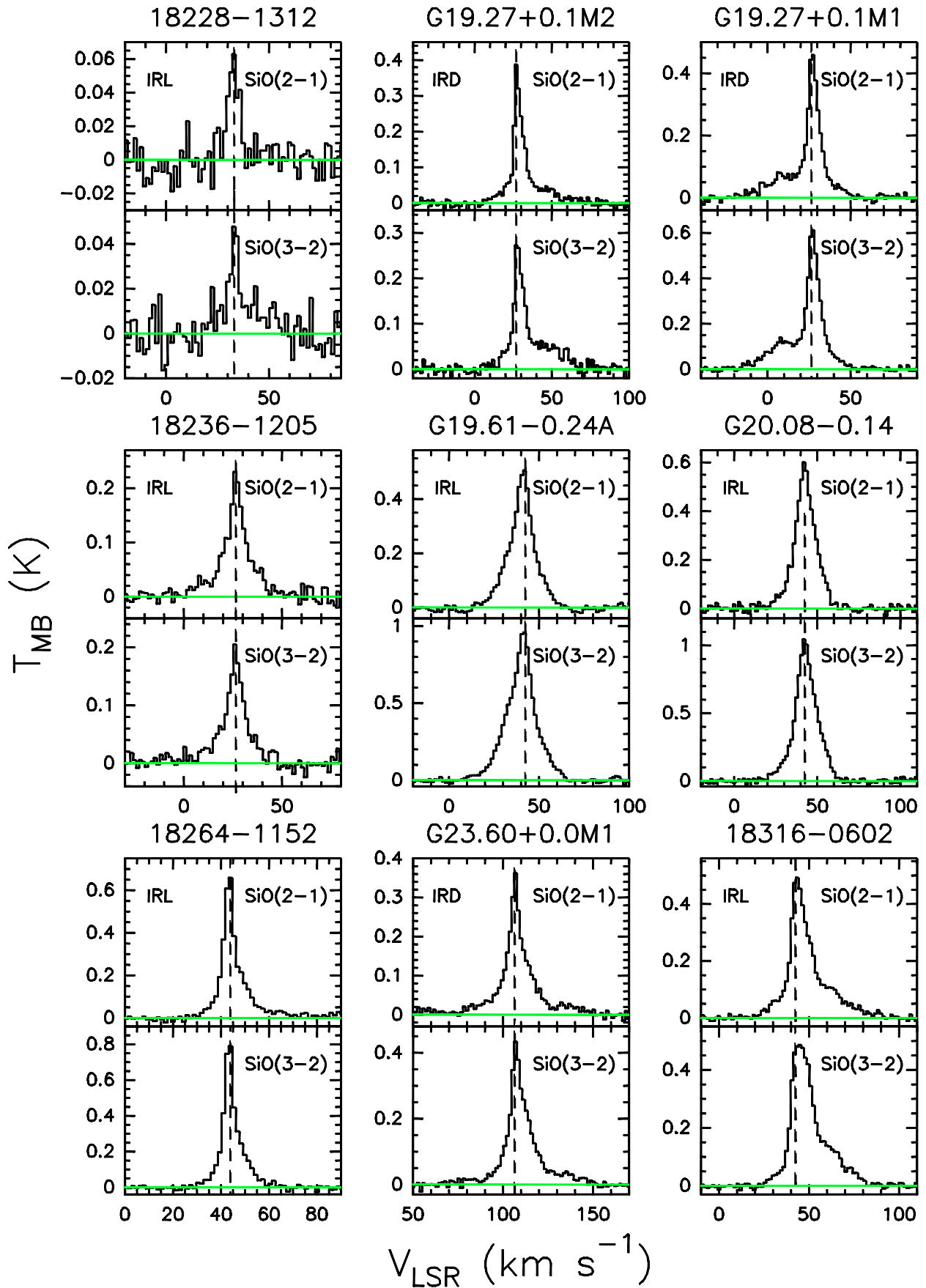


Fig. B.2. continued.

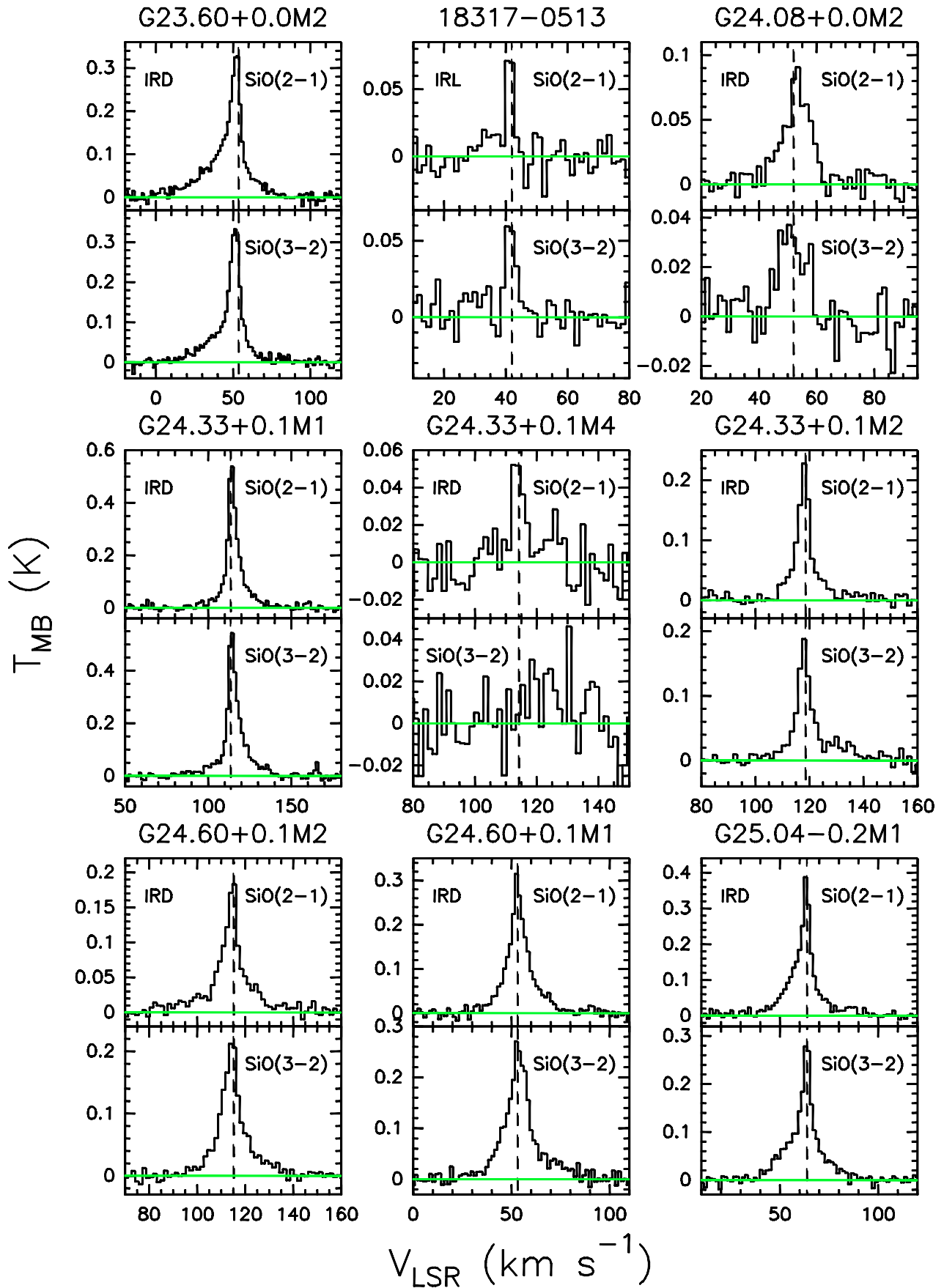


Fig. B.2. continued.

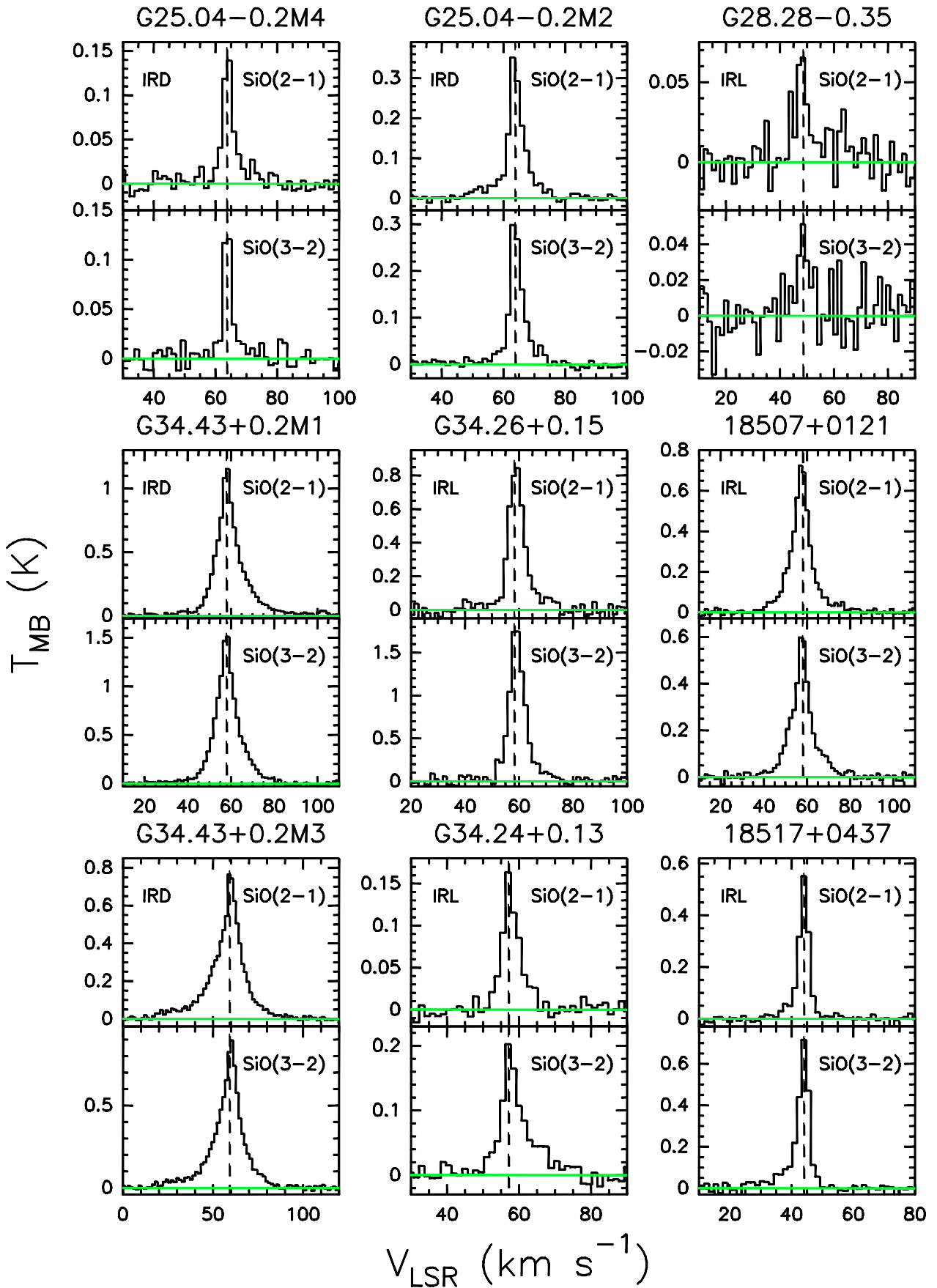


Fig. B.2. continued.

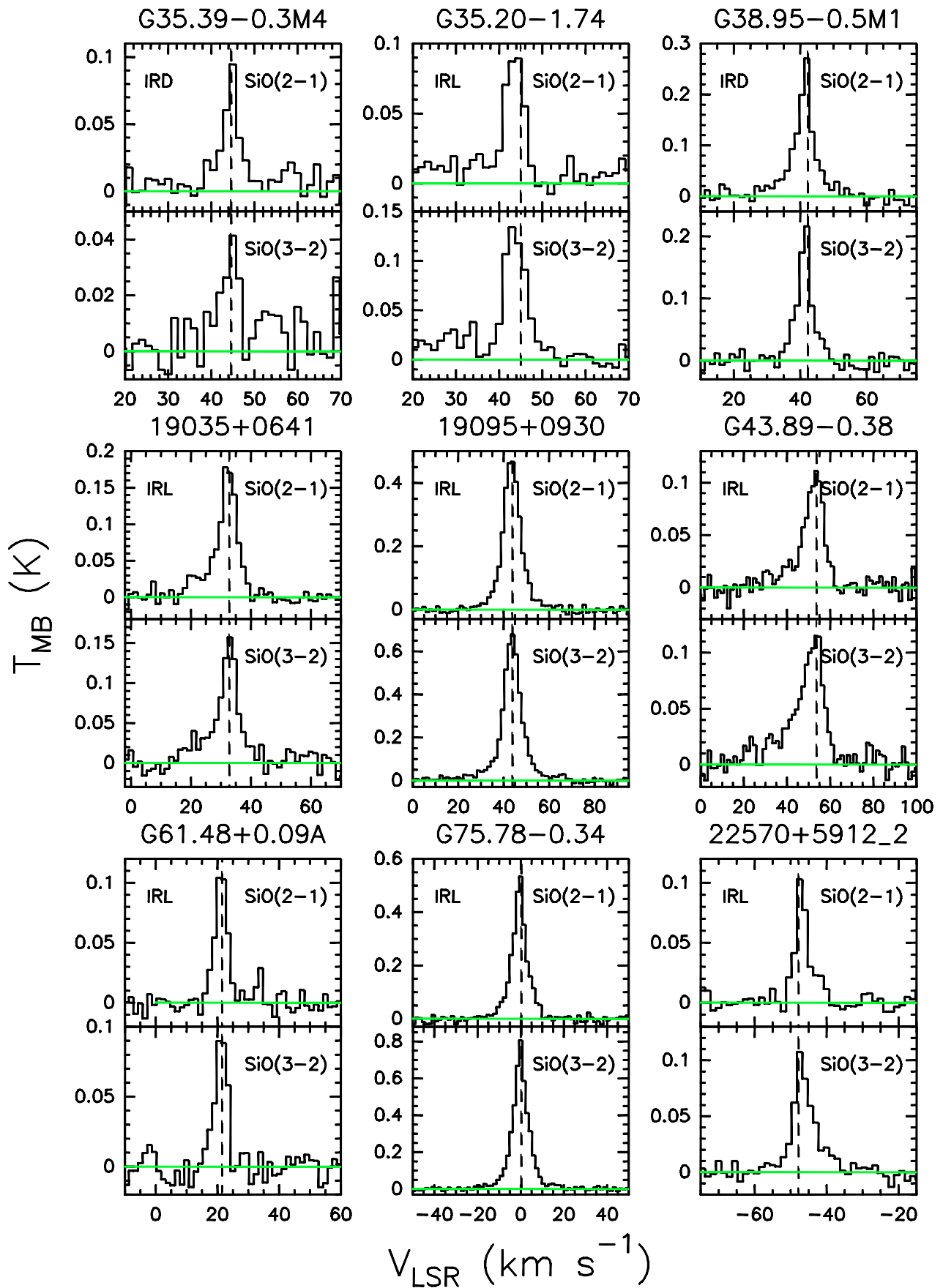


Fig. B.2. continued.

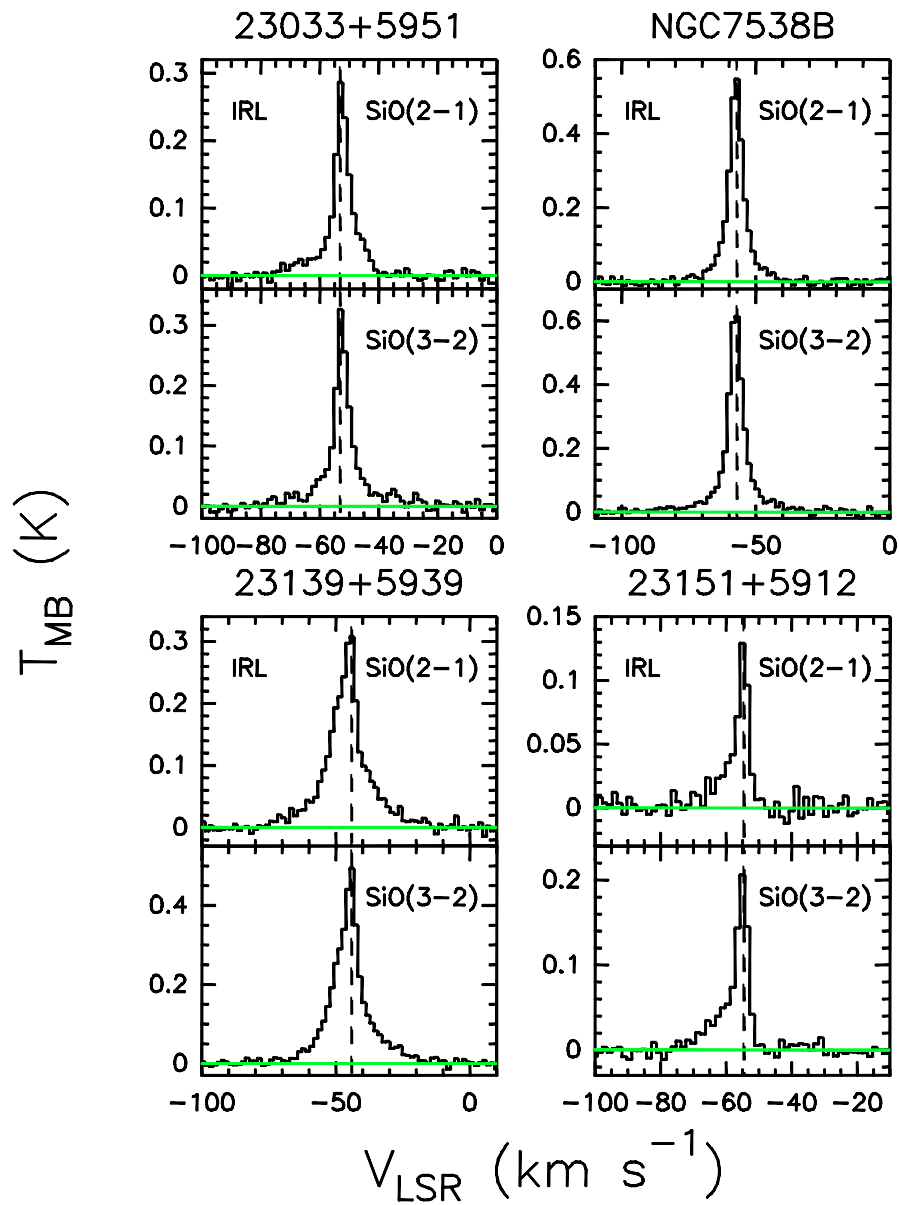


Fig. B.2. continued.